

Article

# Attenuated Total Reflection at THz wavelengths: peculiarities of total internal reflection and polariscopy

Meguya Ryu<sup>1,2</sup>, Soon Hock Ng<sup>3</sup>, Vijayakumar Anand<sup>3</sup>, Stefan Lundgaard<sup>3</sup>, Jingwen Hu<sup>3</sup>, Tomas Katkus<sup>3</sup>, Dominique Appadoo<sup>4</sup>, Zoltan Vilagosh<sup>5</sup>, Andrew W. Wood<sup>5</sup>, Saulius Juodkazis<sup>3,6</sup>, Junko Morikawa<sup>2</sup>

<sup>1</sup> Research Institute for Material and Chemical Measurement, National Metrology Institute of Japan (AIST), Tsukuba Central 3, 1-1-1 Umezono, Tsukuba 305-8563, Japan

<sup>2</sup> CREST - JST and School of Materials and Chemical Technology, Tokyo Institute of Technology, 2-12-1, Ookayama, Meguro-ku, Tokyo 152-8550, Japan

<sup>3</sup> Optical Sciences Centre and ARC Training Centre in Surface Engineering for Advanced Materials (SEAM), School of Science, Swinburne University of Technology, Hawthorn, Vic 3122, Australia

<sup>4</sup> Australian Synchrotron, THz Far Infrared Beamline, Clayton, Vic 3168, Australia

<sup>5</sup> Australian Centre for Electromagnetic Bioeffects Research, Swinburne University of Technology, Hawthorn, Vic 3122, Australia

<sup>6</sup> World Research Hub Initiative (WRHI), School of Materials and Chemical Technology, Tokyo Institute of Technology, 2-12-1, Ookayama, Meguro-ku, Tokyo 152-8550, Japan

\* Correspondence: ryu.m.ab@m.titech.ac.jp (M. R.), sjuodkazis@swin.edu.au (S. J.), morikawa.j.aa@m.titech.ac.jp (J. M.)

Correspondence: ryu.m.ab@m.titech.ac.jp (M. R.), sjuodkazis@swin.edu.au (S. J.), morikawa.j.aa@m.titech.ac.jp (J. M.)

**Abstract:** Capabilities of the Attenuated Total Reflection (ATR) at THz wavelengths for increased sub-surface depth characterisation of (bio-)materials is presented. The penetration depth of a THz evanescent wave in biological samples is dependent on the wavelength and temperature and can reach 0.1-0.5 mm depth due to strong refractive index change  $\sim 0.4$  of the ice-water transition; this is quite significant and important when studying biological samples. Technical challenges are discussed when using ATR for uneven, heterogeneous, high refractive index samples with possibility of frustrated total internal reflection (a breakdown of the ATR reflection-mode into transmission-mode). Local field enhancements at the interface are discussed with numerical/analytical examples. Maxwell's scaling was used to model behaviour of absorber-scatterer inside materials at the interface with ATR prism for realistic complex refractive indices of bio-materials. Modality of ATR with polarisation analysis is proposed and its principle illustrated, opening an invitation for its experimental validation. The sensitivity of the polarised ATR mode to the refractive index between the sample and ATR prism is revealed. Design principles of polarisation active optical elements and spectral filters are outlined. The results and concepts are based on experiments carried out at the THz beamline of the Australian Synchrotron.

**Keywords:** ATR, THz, synchrotron radiation, diagnostics, polariscopy, four polarisation method

## Contents

<b>1</b>	<b>Introduction</b>	<b>2</b>
<b>2</b>	<b>Experimental: THz beamline at Australian synchrotron</b>	<b>2</b>
<b>3</b>	<b>What to consider in ATR measurements?</b>	<b>3</b>
3.1	Attenuated Total Reflection	3
3.2	A useful condition when ATR becomes invalid	4

3.2.1	Example: water in butter around water freezing conditions . . . . .	6
3.3	Polarisation and field enhancement at the interface of ATR prism . . . . .	7
3.4	Four-polarisation (4-Pol) method for ATR . . . . .	8
3.5	Combined spectral filters and polarisers . . . . .	12
<b>4</b>	<b>Conclusions and Outlook</b>	<b>13</b>
	<b>References</b>	<b>14</b>
<b>A</b>	<b>Phase and amplitude changes in ATR</b>	<b>15</b>

## 1. Introduction

There is a particular advantage to use the attenuated total reflection (ATR) technique at THz wavelengths, where water absorption can be detrimental to free space THz beam propagation. With minimal sample preparation, its placement onto an ATR diamond window (in this study) offers a simple and effective method of material characterisation. Harnessing the THz portion of synchrotron radiation, high brightness THz beams are extended to  $< 300 \text{ cm}^{-1}$  wavenumbers (single digit THz frequencies) where conventional tabletop Fourier transform IR (FTIR) spectrometers are rendered less useful due to low signal-to-noise ratio (SNR). The high brilliance of THz synchrotron radiation makes it especially promising for real time monitoring of phase transitions. Due to high transparency of diamond at THz frequencies characterisation of phase transitions can be extended to an anvil or pressure cell (using diamond windows) experiments with materials at high pressure and temperature, recently demonstrated with a 35 MPa cell [1].

The water-ice transition is of particular interest for cryogenic applications in biological materials. It can also be studied and exploited using the ATR technique for deeper characterisation of bio-samples. Due to both a large refractive index change from the water-ice transition ( $\sim 0.4$ ) and change in absorption coefficient through the THz range, the ATR condition can be not fulfilled, i.e., instead of reflection from diamond-sample interface, THz beam propagates in transmission. The refractive index of ice is  $\sim 1.7$  at 1-to-3 THz, increases to  $\sim 1.9$  at 4.2 THz, reduces slowly to 1.75 at 6.5 THz, then quickly drops to 1.1 by 6.9 THz [2]. This means that between 1 and 3 THz, there is a good refractive index contrast between liquid water and ice. Due to the air gaps between sample and ATR diamond window, light tunneling can take place, also contributing to the transmission mode. Addressing these issues and taking advantage of (some of) them is discussed in this prospective/concept paper with numerical examples and required analytical expressions.

In this perspective/concept paper, based on recent experiments at the THz beamline at the Australian synchrotron, technical peculiarities of the ATR operation mode are detailed. We introduce the concept of a four polarisation (4-Pol) method for the ATR mode and numerically validate it. Challenges of multi-reflection beam delivery to (and from) the sample in ATR measurements, as well as ATR condition changes with liquid-solid water transition, are scrutinised in order to extract useful orientation characterisation of samples in ATR experiments. Polarisation, intensity and spectral filtering of complex synchrotron THz radiation can provide more flexibility in material characterisation.

## 2. Experimental: THz beamline at Australian synchrotron

THz/Far-IR beamline at the Australian Synchrotron (first light 2007) was used in this study. Polarisation of synchrotron radiation has combination of a linear (along the extraction mirror slit) and circular polarisations [3]. These two components are due to constant and changing magnetic field through and at the entrance and exit of a bending magnet (the dipole- and edge-emissions, respectively). The THz and IR microscopy beamlines share the synchrotron radiation extracted from the magnet. The THz/Far-IR beamline receives mainly the edge-emission; bunch compression can be achieved to produce coherent synchrotron radiation (CSR) resulting in a flux increase of 2-3 orders in magnitude between  $15\text{-}25 \text{ cm}^{-1}$  (0.45-0.75 THz; 667- 400 nm).

Polarisation is defined in the plane of incidence as  $E_s$  and  $E_p$ , which are  $\perp$  and  $\parallel$  to the plane (or TE and TM modes), respectively (Fig. 1(a)). For anisotropic samples, those two components will be absorbed differently, i.e., alignment of the absorbing dipoles. This opens up the possibility for determining anisotropy of absorbance in the sample. The s-pol. (TE or  $E_y$ ) probes the orientation of dipoles in the plane of ATR window. With low refractive index ( $n_1 < 1.6$ ) samples, which is typical for bio-materials, the reflected light at a typical  $45^\circ$  incidence usually does not experience a phase change upon reflection at the sample-prism interface. However, the p-pol. (TM;  $E_z$ ), which probes the absorbance in the direction perpendicular to the prism-sample interface has a strong dependence of the reflected phase on  $n_1$ . At  $\theta_i = 45^\circ$  incidence, a phase change of  $\pi$  occurs when  $\theta_B < \theta_i < \theta_c$  ( $\theta_B$  and  $\theta_c$  are the Brewster and critical angle, respectively) and the reflected  $E_z$  component becomes  $E_y$ . The consequence of the phase dependence of the TM mode makes polarisation analysis of ATR signals complicated, and most of the published data does not discriminate polarisation for excitation and does not carry out polarisation analysis at the exit after the sample.

A Bruker IFS 125/HR Fourier Transform spectrometer (Bremen, Germany), with a Si bolometer and a single reflection ATR unit (Pike Technologies Inc.) equipped with a diamond crystal/prism (refractive index of  $n_1 = 2.42$ ) modified for vacuum operation was used. A beamsplitter was used to select spectral window of interest. The used ATR unit that had the capability for temperature control by a heater/cooler placed around the diamond ATR prism Fig. 1(a)). Data analysis was carried out with OPUS 8.0 software (Bruker Optik GmbH, Ettlingen, Germany). Under frustrated total internal reflection conditions, the transmitted wave was reflected by a gold plated mirror with varied separation from the ATR diamond crystal surface. In this way, the reflection was redirected back to the ATR detector. The experiments were conducted over the frequency range of 0.18 to 3 THz due to the high resolution and high brightness of synchrotron radiation over this frequency window.

### 3. What to consider in ATR measurements?

#### 3.1. Attenuated Total Reflection

The technique of attenuated total reflection (ATR) spectroscopy has become a popular method to measure dielectric properties of materials. It relies on the reduction of the reflected signal intensity at the total reflection angle, i.e. there is no transmitted wave into the sample (placed on top of the ATR prism). The technique relies on the incident energy being absorbed via an evanescent wave generated at the interface between the sample and prism. The advantage of the method lies in the fact that solid and liquid samples can be studied with minimal preparation. This is exceptionally useful for the THz spectral window since free space propagation of THz radiation under normal conditions is strongly attenuated due to absorption by water vapor. The observed ATR spectrum is noted to be nearly equivalent to that of the transmission type, which suggests that the technique is sampling the absorption coefficient of the sample at the given frequency. If the absorption of the evanescent wave is negligible, the penetration depth of the evanescent E-field ( $1/e$ -level) is given by [4]:

$$d_p^{(ev)} = \frac{\lambda}{2\pi n_1 \sqrt{\sin^2 \theta_i - \left(\frac{n_2}{n_1}\right)^2}}, \quad (1)$$

where  $\lambda$  is the wavelength,  $n_1$  and  $n_2$  are the real parts of the refractive index of the ATR crystal and sample, respectively, and  $\theta$  is the angle of incidence of the incoming radiation; for the beam intensity  $I = E^2$ , the penetration depth becomes  $d_p^{(ev)}/2$ . Since  $\sqrt{\sin^2 \theta_i - (n_2/n_1)^2}$  has to be a real number,  $n_2 < n_1 \sin \theta_i$  sets the limit on the refractive index of the sample for a given ATR crystal. ATR has found its use at infrared frequencies from 30 to 400 THz, where the  $d_p$  is of the order of  $1 \mu\text{m}$  for biological tissue. At these distances, the total absorption of the evanescent wave at distances in the order of the  $d_p$  is, indeed, negligible. However, at low terahertz frequencies (0.3 to 3 THz) the wavelength  $\lambda$  is on the order of 1.0 - 0.1 mm, which yields a  $d_p$  on the order of 0.02 to 0.2 mm. The absorption of

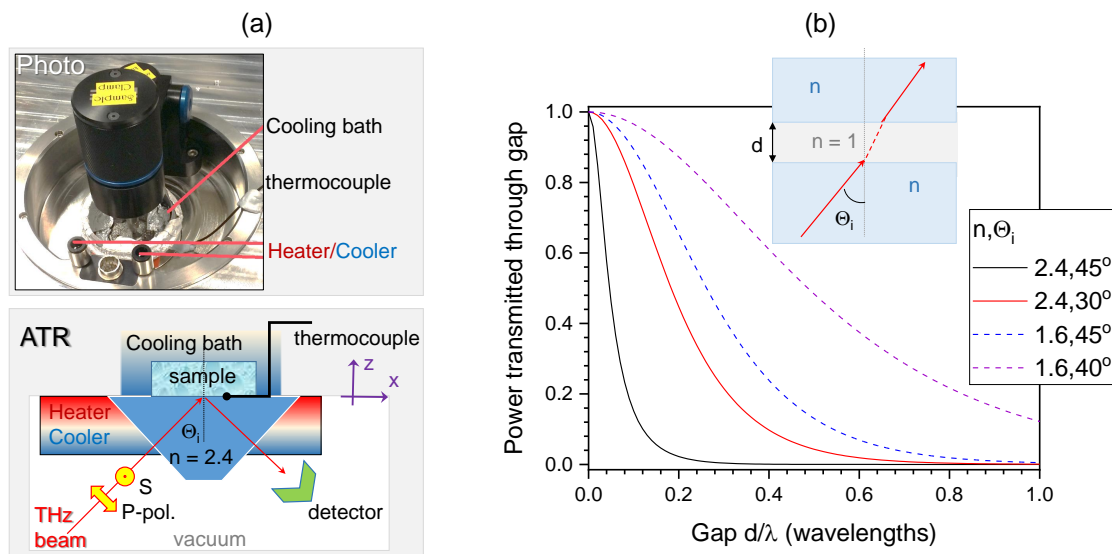


**Figure 1.** (a) Photo and schematics of ATR setup used for temperature dependent absorbance spectroscopy at the THz/Far-IR beamline. (b) Visualisation of frustrated TIR (Eqn. 2) for different angles of incidence and refractive indices  $n$  of the slabs. The index  $n = 1.6$  also corresponds to the case when two  $n = 2.4$  (diamond) slabs are separated by  $n_{gap} = 1.5$  (bio-sample), i.e.,  $\frac{n}{n_{gap}} = \frac{2.4}{1.5} = 1.6$ .

the evanescent wave becomes not negligible at such depths in biological tissues. A more elaborate equation for the reflected wave intensity, using the complex refractive index  $n^* = n + ik$ , where  $k$  is the imaginary part of the complex refractive index  $n^*$  is required when polarisation becomes important.

It is instructive to estimate what are frustrated- total internal reflection (TIR) transmission predictions. This affects the intensity reaching different depths of the sample as well as accounting for the detected THz power losses when an air gap is formed between the sample and ATR prism. The fraction of light intensity polarized in the plane of incidence (p-pol), at the wavelength  $\lambda$ , transmitted across the gap of width  $d$ , with refractive index  $n_{gap} = 1$ , and in the case of ATR prism of refractive index  $n$  is given [5] (Fig. 1):

$$T_p = \frac{1}{\alpha \sinh^2 y + 1}, \quad \alpha = \left( \frac{n^2 - 1}{2n} \right)^2 \frac{[(n^2 + 1) \sin^2 \theta_i - 1]^2}{\cos^2 \theta_i (n^2 \sin^2 \theta_i - 1)}, \quad y = 2\pi \left( \frac{d}{\lambda} \right) \sqrt{n^2 \sin^2 \theta_i - 1}, \quad (2)$$

where  $\theta_i$  is the angle of incidence onto the first surface (ATR prism); the same material of refractive index  $n$  is considered on the both sides of the gap. This set of formulas also shows that larger light penetration depth can be achieved if a sample on ATR prism has high refractive index inclusions.

We demonstrated the ATR technique for determination of THz penetration depth into bio-materials at different temperatures using synchrotron radiation (the Australian Synchrotron) in the frustrated reflection mode with Au-mirror placed above the 2-mm-thick sample [6,7].

### 3.2. A useful condition when ATR becomes invalid

When measuring reflection of THz radiation in the ATR geometry at  $\theta_i = 45^\circ$ , the ratio of the refractive indices of the diamond prism  $n_1 = 2.42$  and sample  $n_2$  is important since the ATR occurs at  $n_1 \sin \theta_i > n_2$  (Eqn. 4). This sets  $n_2 < 1.71$  and is critically important in characterisation of bio-materials close to this ATR condition (a heating/cooling compatible ATR unit is shown in Fig. 2(a-b)). With water  $n_2 \approx 2.1$  and ice  $n_2 \approx 1.7$  at  $\approx 1$  THz, direct transmission into the sample takes place (Fig. 2(c)). This change of refractive index can be exploited for better depth characterisation of materials due to the larger penetration depth of the evanescent field and direct transmission into the sample. The latter case requires modification of the measurement technique via the addition of a top reflecting mirror

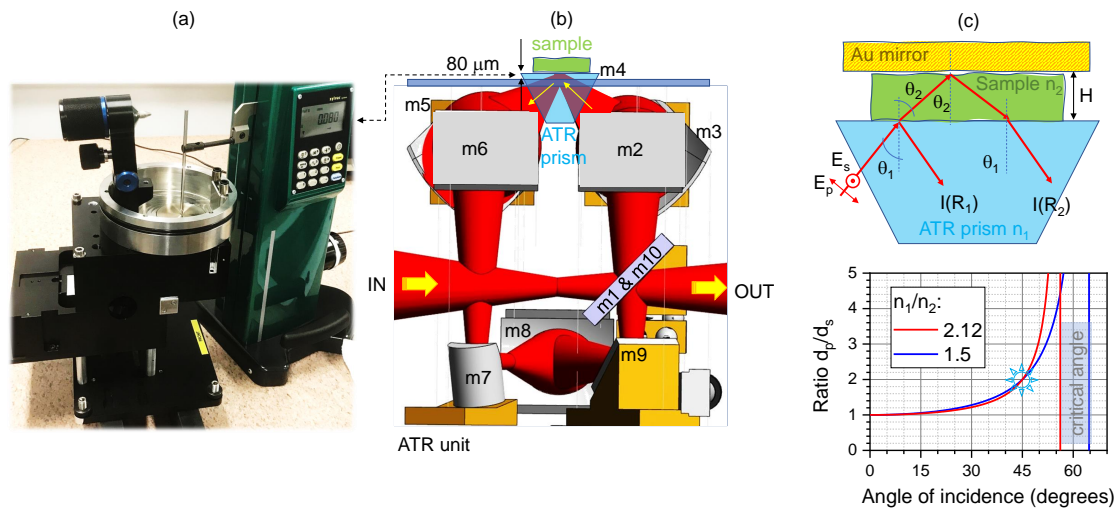


**Figure 2.** (a-b) Photo and schematics of the beam path in ATR unit. Three reflections are encountered from the IN-port to the sample (mirrors m1-3) and extra six for the path sample-to-OUT port (m5-10). (Image: courtesy Dr. Jeff Kuehl) (c) Schematics of measurements with top reflecting mirror when TIR conditions are not fulfilled due to the high refractive index  $n_2$  of the sample. Plot shows the evanescent field ratio for the p-pol. (TM) and s-pol. (TE)  $d_p/d_s$  (Eqn. 3) vs the angle of incidence  $\theta_i$ . For the non-polarised illumination, the penetration depth of evanescent field is  $d_{ev} = \frac{d_s + d_p}{2}$ . Critical angle is at  $\theta_c = \arcsin(\frac{n_2}{n_1})$ .

to redirect THz radiation back to the detection direction along the ATR geometry (Fig. 2(c)) as we introduced recently [6].

The optical path length  $l_T$  in the case of transmission mode in the ATR setup is defined by the distance,  $H$ , to the mirror (see drawing in Fig. 2(c)) as  $l_T = 2H / \cos(\theta_2)$  (from Snell's law  $n_1 \sin(\theta_1) = n_2 \sin(\theta_2)$  and the Pythagorean identity of sin and cos functions one finds  $\cos \theta_2 = \sqrt{1 - (\frac{n_1}{n_2} \sin \theta_1)^2}$ ). Precise determination of  $H$  is important since the working surface of ATR prism and sample housing unit usually have height differences of tens-of-micrometers Fig. 2(a-b). Power reflected at the first prism-sample interface is  $I(R_1) = R I_{in}$ , where  $R$  is the energy reflection coefficient and  $I_{in}$  is the incident power. Considering a perfect reflection  $R_{Au} = 1$  at the top-mirror, the power re-directed back to the detector is  $I(R_2) = (1 - R)^2 I_{in} \exp(-\alpha l_T)$ .

The experimentally measured ratio  $X_{exp} \equiv \frac{Power_{Sample/Diamond}}{Power_{Air/Diamond}} = (I(R_1) + I(R_2)) / I_{in} = R + (1 - R)^2 \exp(-\alpha l_T)$ . The absorption (optical losses) coefficient is then  $\alpha = -\frac{\cos(\theta_2)}{2H} \ln \left( \frac{X_{exp} - R}{(1 - R)^2} \right)$ . The reflectivity coefficient (power, intensity) is defined by the angle of incidence  $\theta_i$  and the complex refractive indices of sample and ATR-prism  $\tilde{n} = n + i\kappa = \sqrt{\epsilon}$ , where  $\epsilon$  is the permittivity.

For the normal incidence and lossless ATR diamond prism ( $n_1, \kappa_1 = 0$ ), the reflectivity from the sample ( $n_2, \kappa_2$ ) is  $R = [(n_1 - n_2)^2 + \kappa_2^2] / [(n_1 + n_2)^2 + \kappa_2^2]$  and the absorbed part of energy is  $A = 1 - R$  since there is no transmission  $T = 0$ . The Beer - Lambert law defines the transmitted part  $T = e^{-\alpha l_T}$  in a single pass through thickness  $l_T$ ;  $\alpha l_T \equiv \ln(10) OD$ , where the optical density (absorbance) is calculated from transmittance  $OD = -\lg T$  (note, this expression can be used for back-reflected signals in the ATR-setup with a top mirror when transmission is collected in the reflection direction and ATR condition is not satisfied). For an arbitrary angle of incidence  $\theta_i$ , the reflectivity for s-/p-pol. can be expressed as  $R_s = r_s^2 = \left( -\frac{\sin(\theta_1 - \theta_2)}{\sin(\theta_1 + \theta_2)} \right)^2$  and  $R_p = r_p^2 = \left( \frac{\tan(\theta_1 - \theta_2)}{\tan(\theta_1 + \theta_2)} \right)^2$ , the Fresnel's sine and tangent laws, respectively.

The described measurement with invalid ATR condition using a top-mirror allows deeper material interrogation, owing to the absorption from a much longer optical path as compared to that probed by

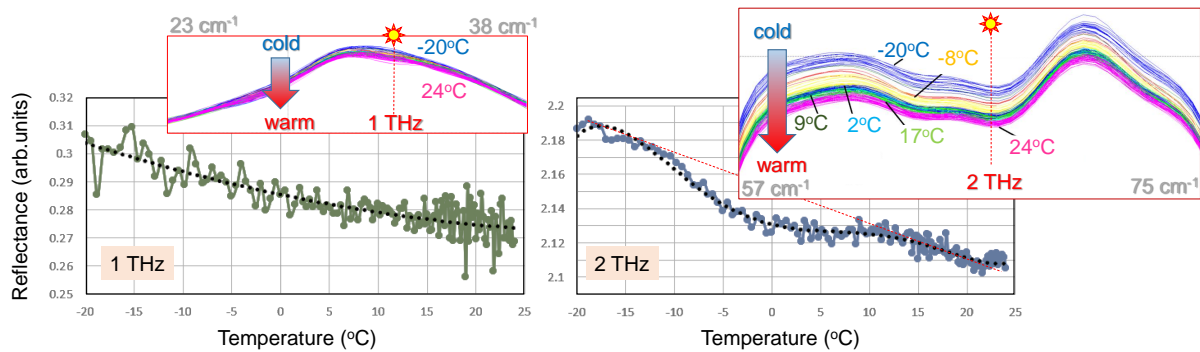


**Figure 3.** Temperature dependence of butter sample (2-mm-thick) at 1 and 2 THz measured with Au top-mirror [7]; wavelength of 1 THz is 0.3 mm and 2 THz is 0.15 mm. The insets shows reflectance intensity vs wavenumber; air (no Au top-mirror) reflectance was taken as the reference. Dotted-lines (black) are eye guide splines of the experimental data.

the evanescent field (at ATR conditions) as shown in the plot in Fig. 2(c). The penetration depth into sample at ATR conditions is sub-wavelength and the s-pol. is probing half the depth as compared to p-pol. at the specific  $\theta_i = \pi/4$  incidence, regardless the relative refractive index  $\frac{n_1}{n_2}$ . The penetration depth for s- and p-polarisations is [4]:

$$d_s = \frac{\lambda_0}{n_1} \frac{n_{21} \cos \theta_i}{\pi(1 - n_{21}^2) \sqrt{\sin^2 \theta_i - n_{21}^2}}, d_p = \frac{\lambda_0}{n_1} \frac{n_{21} \cos \theta_i [2 \sin^2 \theta_i - n_{21}^2]}{\pi(1 - n_{21}^2) [(1 + n_{21}^2) \sin^2 \theta_i - n_{21}^2] \sqrt{\sin^2 \theta_i - n_{21}^2}}, \quad (3)$$

where  $n_{21} = n_2/n_1$  (sample/prism),  $\lambda_0$  vacuum wavelength,  $\theta_i$  is the angle of incidence onto the prism-sample interface.

### 3.2.1. Example: water in butter around water freezing conditions

The THz-ATR technique with a top-reflecting gold mirror was used to measure absorbance of bio-materials [7]. At the chosen  $\sim 0.7 - 2.2$  THz synchrotron radiation band, polarisation is mostly linear and corresponds to the s-pol. at the sample-prism interface. Freezing water reduces its real part of refractive index only slightly ( $n$  is proportional to mass density  $\rho$ ), however a very strong reduction in absorption occurs. Experimental values of ice reflectivity [8–10] show a significant increase at the  $56.5\text{--}75.0 \text{ cm}^{-1}$  window (1.70–2.25 THz). Up to three times difference between reflectivity of water ( $\sim 4\%$ ) and ice ( $R > 12\%$ ) to that from air was observed [8–10].

Lurpak butter had 14.7% w/w water, 3% w/w non-fatty solids, which are dissolved in the water and the rest is fat [11]. The temperature was varied from  $-20$  to  $24^\circ\text{C}$  over a total time frame of 24 min with continual scanning; a total of 140 sets of 40 averaged scans were collected during that time span. Figure 3 shows reflectance evolution with temperature at two spectral regions. The inset presents reflectivity changes with temperature. There is a featureless temperature dependent reduction variation with butter which is evident at the most sensitive frequency range of 0.95 to 1.0 THz. Considerably more strong temperature dependence of reflectivity was observed at 2 THz band. Overall, the reflected ATR signal for Lurpak butter showed a 13% decrease for over the  $-20^\circ\text{C}$  to  $+24^\circ\text{C}$  change at 1.0 THz and a 3.5 % decrease at 2 THz. A slight decrease in reflectance with temperature variation  $\pm 20^\circ\text{C}$  around water freezing is indicating that the water content  $\sim 14.7\%$  needs to be regarded as being “bound” in a homogenous mixture of fat and protein. The temperature related reduction in reflectance in the region of 2.0 THz showed a plateau in the  $2\text{--}12^\circ\text{C}$  range. It may be related to a transition in the constituent fats. These results would suggest that other materials with bound water may not show the effect of water freezing.

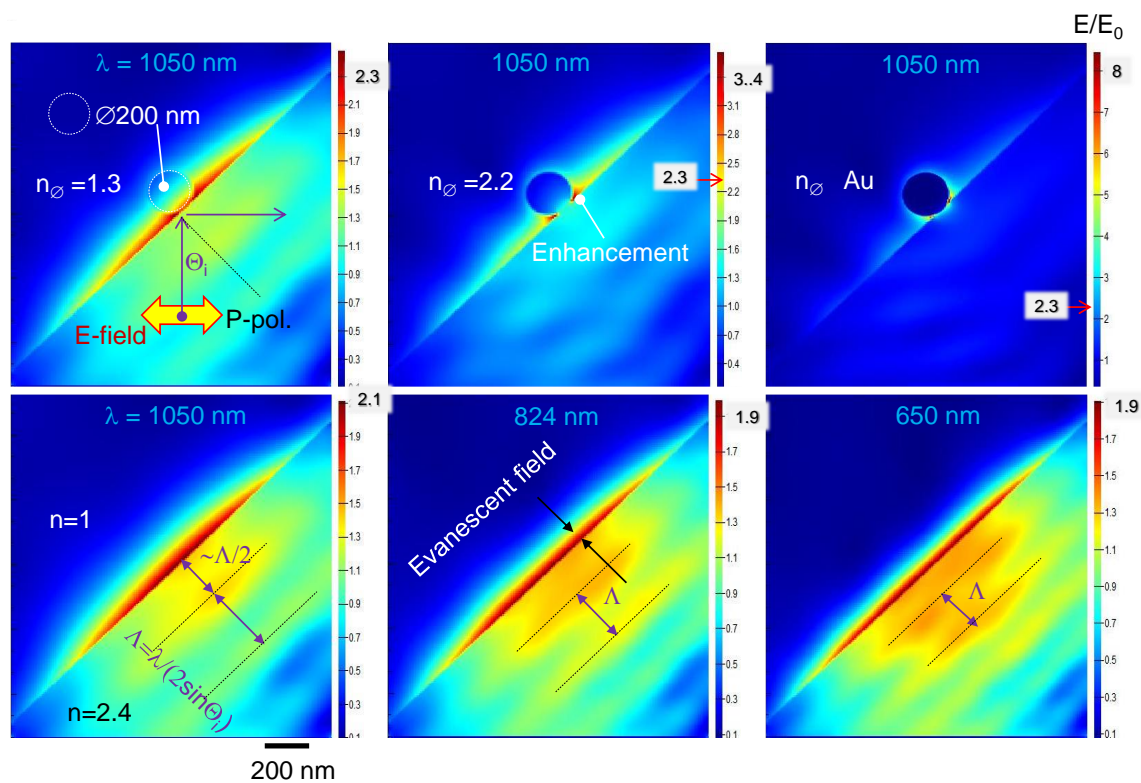


**Figure 4.** Maxwell's scaling (change nm to  $\mu\text{m}$  for the same refractive index): numerical Finite Difference Time Domain (FDTD; Lumerical Solutions) calculations for optical wavelengths of  $\lambda = 1 \mu\text{m} - 0.65 \mu\text{m}$  to simulate evanescent field at the ATR geometry used (at THz radiation) and at the angle of incidence of  $\theta_i = 45^\circ$  (ATR interface is  $45^\circ$ -tilted). Top-row shows E-field enhancement when a  $\sim \lambda/20$ -diameter sphere of refractive index  $n = 1.3$  (water or ice at visible),  $2.2$  (water or ice at THz) and gold (Au) touches the ATR prism of  $n = 2.4$  (diamond); all intensity maps were calculated for the same wavelength  $\lambda = 1050 \text{ nm}$ . Bottom-row shows evanescent field at the interface of  $\lambda = 1 \mu\text{m} - 0.65 \mu\text{m}$ ; the interference maxima are recognisable in the  $n = 2.4$  media (wavelength there is  $\lambda/n$ ). Calculations were carried for p-pol. E-field with strength  $E_0 = 1$ , hence  $E/E_0$  scale represents enhancement.

### 3.3. Polarisation and field enhancement at the interface of ATR prism

A unique feature of ATR geometry is that the maximum intensity of incident beam, regardless of its polarisation, is localised at the interface (see details below and Fig. 4). This is defined by the conditions when light propagates from high-to-low refractive index (even at low angles of incidence when the ATR condition is not fulfilled). For normal beam propagation from low-to-high index (incidence from air), the intensity maximum is  $\lambda/4$  above the surface due to interference between the incident and reflected beams. Maximum intensity at the interface using the back-side illumination is used in Raman scattering sensing and light-induced back-side wet etching (LIBWE) in subtractive machining [12,13].

The polarisation of THz beam is not controlled as the beam is delivered to the ATR prism. This is the condition when maximum intensity is obtained on the sample. The experimentally determined polarisation was 90% linear and 10% circular due to sum of the linear and circular polarisations at  $< 100 \text{ cm}^{-1}$ . This translates to the prevailing s-pol. on the sample placed on the ATR window for the measurements. For wavenumbers larger than  $100 \text{ cm}^{-1}$ , the ratio linear-to-isotropic polarisation was 20%-to-80%.

For ATR measurements, the depth of the evanescent field is larger for the p-polarisation as compared with s-pol (Fig. 2(c); Eqn. 3). It is important in the case of frustrated total internal reflection

(TIR) modeled for the non-polarised light by Eqns. 2 (see Fig. 1(b)). Also, E-field enhancement for the component of the E-field perpendicular to the interface between two dielectrics can be harnessed. Indeed, the boundary conditions of Maxwell equations requires that the normal component of the displacement  $D_n = \epsilon E_n$  be continuous across the boundary (when there are no surface charges),  $\epsilon$  is the permittivity at the corresponding wavelength; the  $E_n = E_{p-pol} \cdot \cos \theta_i$ . Hence, the  $D_n$  in both the air and diamond are the same, which defines the E-field enhancement  $E_{air} = \frac{\epsilon_{diamond}}{\epsilon_{air}} \times E_{diamond} \approx 2.4^2 E_{diamond}$ , since  $n = \sqrt{\epsilon}$ . Note, here we assume the E-field inside the ATR prism as a reference to calculate enhancement at the air - diamond interface (on the air side). For comparison, reflection at the normal incidence from vacuum onto the diamond prism with  $n = 2.4$  has  $R = \frac{(n-1)^2}{(n+1)^2} \approx 17\%$  defining the transmitted  $T = 1 - R$  fraction of THz radiation (would be inside the ATR prism).

The penetration depth of the evanescent field depends on the the wavelength of light in ATR geometry (see the bottom row in Fig. 4). Intensity distribution in the case of frustrated TIR depends on the normalised gap  $d/\lambda$  (Eqn. 2; Fig. 1(b)). It shows that depending on the angle of incidence and refractive indices, light transmission can take place only when gaps are sub-wavelength. In standard ATR measurements, such frustrated TIR conditions can take place due to presence of structures and different inclusions of higher refractive index in the sample. The wavelength scaling in frustrated TIR gives insights into light tunneling regardless of the wavelength. Based on this Maxwell's scaling it is useful to model light transmission, reflection and enhancement at the interface of ATR prism using finite difference time domain (FDTD) calculations (Lumerical solutions). Figure 4 shows the results for the IR-visible spectra range, however, the predictions are universal as long as the refractive index is the same. To model a sub-wavelength inclusion inside a sample, a sub-wavelength diameter sphere of different refractive index: dielectric (1.3 and 2.2) as well as metallic (Au) were chosen. Without the sphere, localisation of the evanescent field at the interface protruding into air gap for length comparable with  $\lambda/4$  is clearly recognisable. An extra enhancement of the local E-field at the interface occurred in the nano-gap regions around the sphere. This is an illustration of the E-field enhancement of the normal  $E_n$  component discussed above. For the ATR measurements, the local field enhancement around inclusions of difference refractive indices would cause a stronger contribution from those regions where light intensity was larger. Overall, the volume where the light field intensity is augmented around a sub-wavelength inclusion increases (see the same intensity  $E = 2.3$  markers in the top-row maps in Fig. 1(a)).

### 3.4. Four-polarisation (4-Pol) method for ATR

The four-polarisation (4-Pol) method [15] allows determination of orientation of the absorbing molecular dipoles in the IR fingerprinting spectral range. It can be used to observe complex molecular arrangement using microscopy and, when combined with high brightness synchrotron radiation, opens the possibility to observe the change of molecular ordering during phase transitions and crystallisation in real time. It was implemented to reveal molecular ordering in paracetamol (type-II) micro-crystals which are better soluble in water [16]. The principle of measuring absorbance at four sample orientations (or beam polarisation) using linearly polarised light is applicable to any spectral range. Patterns of sub-wavelength,  $\lambda/50$ , features can be revealed by measuring angular dependence of absorbance/transmittance [17]. Separation of transmittance changes due to birefringence,  $\Delta n$ , and dichroism,  $\Delta \alpha$ , in polariscopy (with aligned polariser and analyser) can be realised due to difference in angular dependence of those two contributions using the 4-Pol technique [18].

We conjecture here that the 4-Pol method of orientational probing of absorbance could be also adopted for ATR with one light E-field oriented in the plane of prism surface (s-pol.) and another perpendicular to it (the evanescent field of incident p-pol.). Developing the 4-Pol method for ATR is next motivation for experiments on the THz beamline at the Australian Synchrotron. The conjecture is based on basic principles of polarisation analysis and is applicable to any wavelengths in ATR measurements.

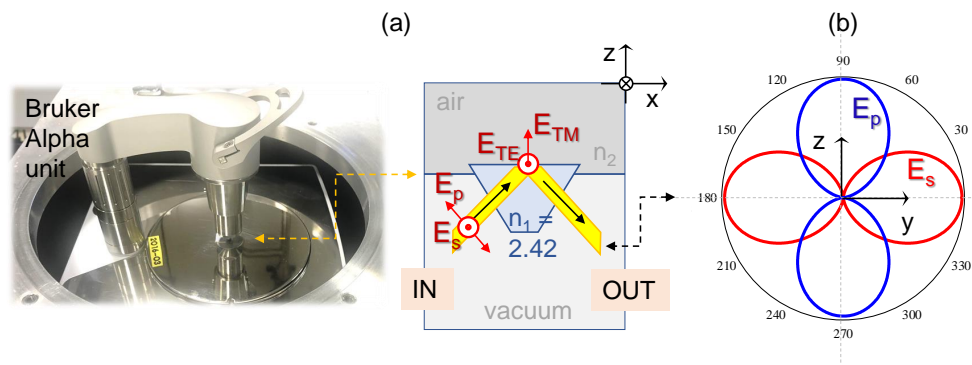


**Figure 5.** (a) Geometry and conventions of ATR; photo of Bruker Alpha unit setup on the THz-beamline compartment. ATR conventions: incident beam (IN) has  $E_{s,p}$  polarisations selected by a wire grid polariser incident on the ATR diamond ( $n_1 = 2.42$  [14]) prism; plane of incidence is  $xz$ . The reflected beam is elliptically polarised due to phase and amplitude changes incurred upon reflection (e.g., air case  $n_2 = 1$ ). The sample is contributing with absorption and phase change for the output beam (OUT). At the interface (sample) the evanescent field  $E_{TM}$  (or  $E_z$ ) and  $E_{TE}$  or ( $E_y$ ) defines the light-matter interaction. (b) The reflected beam can be expressed via  $E_{s,p}$  projections measured analyser and given by Eqn. 4. The angle  $\varphi$  is the orientation of the wire grid polariser in the incidence side (IN);  $\varphi = 0^\circ$  corresponds for pure  $E_s$  component incident onto the ATR prism. The amplitude span in the polar plot is [0-1]. The two components of the  $E_p$  and  $E_s$  are shown separately by the dipole-like figures (each term in Eqn. 4).

To select the required orientation of linear polarisation, a mesh-grid polariser is used. Polarisation is defined in the plane of incidence as  $E_s$  and  $E_p$ , which are  $\perp$  and  $\parallel$  to the plane (or TE and TM modes), respectively. By rotating the mesh-grid polariser by an angle,  $\varphi$ , the linearly polarised power (energy, intensity),  $I$ , in the plane of incidence is defined by  $I \propto E_s^2 \cos^2 \varphi + E_p^2 \sin^2 \varphi$  components;  $\varphi = 0^\circ$  corresponds to the pure  $E_s$  light [3]. Depending on the angle  $\varphi$ , a different ratio of the  $E_z$  and  $E_y$  near-field (Fig. 5) are created in the sample. Those two components will be absorbed differently depending on the anisotropy of the sample, i.e., alignment of absorbers.

The phase and amplitude changes upon ATR reflection (Appendix Sec. A) shows that one would expect an elliptically polarised light emerging from the ATR prism (even without sample, see inset in Fig. A1(b) and Fig. 5). The beam after the prism can be analysed with a linear analyser which is set to determine  $E_s$  and  $E_p$  polarisations. The most general expression of the THz power measured after the ATR prism would be an addition of two perpendicular contributions along the s- and p-polarisations:

$$Power^{(OUT)}(\varphi) = A_s \times E_s^2 \cos^2(\varphi + \Delta\psi_s) + A_p \times E_p^2 \sin^2(\varphi + \Delta\psi_p), \quad (4)$$

where  $A_{s,p}$  are the arbitrary amplitudes accounting for both absorption (losses) and changes in amplitude due to reflection;  $\Delta\psi_{s,p}$  are the phases for s- and p-polarisations, respectively. The angle  $\varphi$  defines the orientation of the linear polarisation in the incident beam, i.e., for  $\varphi = 0^\circ$  only  $E_s$  polarisation is present and  $\varphi = 90^\circ$  corresponds to pure  $E_p$ . When pure  $E_s$  polarisation is incident on the sample and there are no changes in the phase of the reflected beam, the orientational output power will have a horizontally aligned figure-8 (Fig. 5) and, consequently, for the pure  $E_p$  case - the vertical figure-8. When the incident beam has both  $E_s$  and  $E_p$  fields, which are absorbed along  $z$ - (evanescent) and  $y$ -directions, the emerging field can be modeled with the Eqn. 4 where changes of phases are also set as fitting parameters. The phase change upon reflection of s-/p-polarisations (TE/TM modes) are solely defined by the real part of the refractive index.

THz beamline receives  $\sim 20\%$  of a linear  $E_L$  (along the slit of the first mirror) polarisation contributing to  $E_s$  and the rest 80% is isotropic  $E_I$  (circular) contributing to the  $E_s$  and  $E_p$  at frequencies larger than  $\sim 3$  THz [3]. The transmitted power through a metallic linear-grid analyser at the entrance

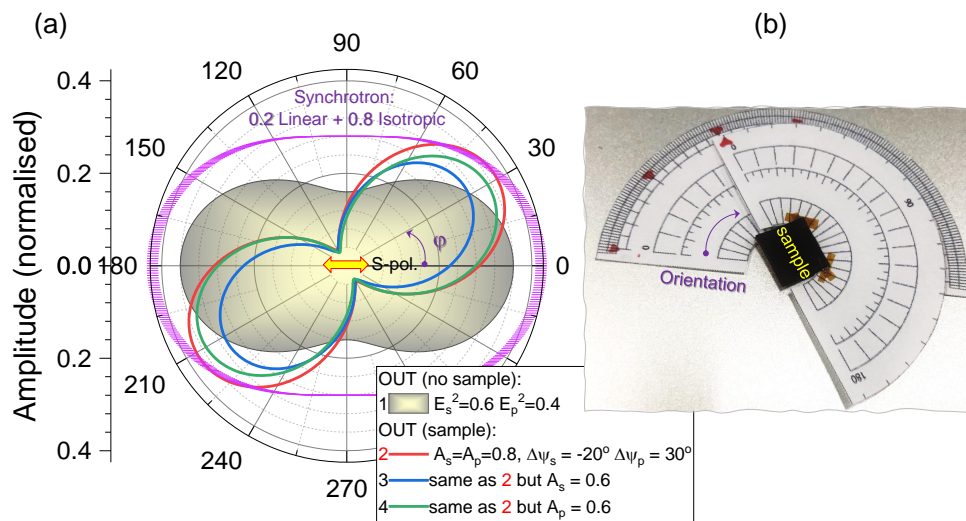


**Figure 6.** Numerical example of polarisation analysis at the ATR output (OUT) based on Eqn. 4. Angular dependence of synchrotron THz radiation (at THz beamline) comprised by 20% of linear polarisation and 80% isotropic (circular) [3] is shown. (b) Sample holder for four-polarisations (4-Pol) ATR measurements: instead of changing linear polarisation of light beam (THz), sample orientation can be changed; sample shown is isotropic THz absorber - black paper.

port  $IN$  to ATR prism is  $Power^{(IN)}(\varphi) = \frac{1}{2}(E_L^2 + E_L^2) + \frac{1}{2}E_L^2 \cos(2\varphi) = \frac{1}{2}(0.2 + 0.8) + \frac{1}{2}0.2 \cos(2\varphi) \equiv 0.5 + 0.1 \cos(2\varphi)$  (shown in Fig. 6(a)). This would be an expected angular distribution at the  $IN$  port if there is no polariser. After the ATR, with no absorption for s- and p-components ( $A_{s,p}$ ) and no phase change ( $\Delta\psi_{s,p}$ ) upon reflection (see Eqn. 4) the same angular dependence would be expected. However, even without any sample the beam reflected from ATR prism will change its polarisation due to phase changes for s-/p-polarisations  $\Delta\psi_{s,p}$ , respectively (Eqn. 4); see Fig. A1(b) where s-pol. (TE) experience an advance of phase by  $\sim \lambda/5$  while the p-pol. (TM) will reduce lag of  $2\pi$  phase by similar amount at  $\theta_i = \pi/4$  angle of incidence on the ATR prism. As a result, just by reflection without any sample, there will be change of polarisation at the OUT port. With sample, the refractive index contrast (real parts) will change those phase shifts. However, any anisotropy in absorbance  $A_{s,p}$  will change the amplitude of the reflected signal at the corresponding polarisation. This would also cause a change in the polarisation of outgoing beam at OUT port. Equation 4 accounts for those all changes.

Figure 6 illustrates the use of Eqn. 4 for analysis of beam at the OUT-port of ATR. Analysis is based on two perpendicular field components  $E_s$  and  $E_p$  with independent amplitudes. Isotropic and anisotropic absorbance changes are accounted for by the coefficients  $A_{s,p}$ . Changes of phases of the s-/p-components with the sample ( $n_2$ ) placed on top of ATR prism ( $n_1$ ) are accounted for by the  $\Delta\psi_{s,p}$ . Isotropic absorbance in y- and z-orientations is presented by the curve 2 with  $A_s = A_p = 0.8$  and phase changes corresponding to reflection from low refractive index material (Fig. A1(b)). Anisotropy along y- or z-direction in the sample is modeled by a 20% change in coefficient  $A_{s,p}$ . As a result, the figure-8 (dipole-like absorbance) is rotated/tilted (an angular shift is introduced). This illustrates that polarisation analysis of ATR results can be a useful tool for measurement of anisotropy in refractive index as well as absorbance by fitting Eqn. 4 with experimentally measured data with polarisation analysis at the OUT-port. The TM-mode can experience strong field enhancement at the interface (Fig. 4) and can cause additional absorption. Sub-wavelength structures at the sample-ATR prism interface cause depolarisation of E-field components, e.g.,  $E_x = \sqrt{[E_s^2 + E_p^2] - (E_y^2 + E_z^2)}$  in the sample's frame of reference (Fig. 5(a)); here the intensity of incident beam is  $E_{in}^2 = E_s^2 + E_p^2$ . The above described polarisation changes in the case of ATR should be possible to determine using polarisation analysis at the OUT port and it will be carried out in future studies.

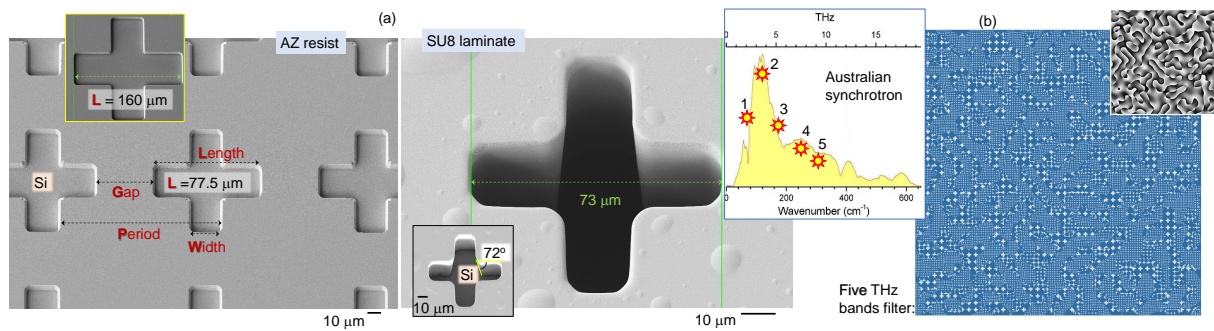


**Figure 7.** (a) SEM images of THz filters defined by photo-lithography:  $\sim 6 \mu\text{m}$ -thick AZ4562 resist (applied on surface) and SU8 laminate 20-500  $\mu\text{m}$  thickness (SU8X from DJ Microlaminates Ltd.; applied or free-standing.) The period, length and width  $P, L, W$  defines the the central wavelength  $\lambda_0$  and the bandwidth  $\Delta\lambda$  of the filter [22]; gap  $G = P - L$ . (b) Superimposed five THz bands filter based of the cross apertures (a). The binary mask (false color) and the  $(0 - 2\pi)$  phase map of the filter (see details in Fig. 8). Spectrum of Australian synchrotron radiation at the THz beamline [23] is shown with selected five frequencies (star-markers).

Equation 4 can be fitted by  $Fit(\varphi) = Amp \times \cos(2\varphi + 2\psi) + Offset$ , which is used for the 4-Pol method (see synchrotron radiation angular distribution in Fig. 6(a) plotted with such dependence). The angle  $2\psi$  indicates orientation of the sample (e.g, absorbing dipoles) and  $Amp = (I_{max} - I_{min})/2$  and  $Offset = (I_{max} + I_{min})/2$  with  $I_{max,min}$  the maximum and minimum intensities of the transmitted or reflected light. By analysing the OUT-port polarisation and using the 4-Pol fit, it should be possible to establish anisotropy in absorbance ( $A_{s,p}$ ) and refractive index ratio  $\frac{n_2}{n_1}$  defining  $\Delta\psi_{s,p}$ . For large samples fitting on 3-mm-window of ATR, sample rotation can be used to realise 4-Pol method (Fig. 6(b)). Visualisation of 4-Pol-ATR method (Fig. 6) is extendable to the hyper-spectral dimension since a broad THz spectrum is recorded. Metallic grid polarisers are polarisation insensitive and by measuring spectra at several angles with the analyser on the OUT-port or by rotating the sample on the ATR prism, sample anisotropy can be examined. One can envisage an ATR geometry where the entire ATR prism with fixed sample can be rotated (around z-axis (Fig. 5)). Such measurements would require a hemispherical or conical ATR prism and could provide more flexible setup, e.g., as it is realised for the synchrotron IR microscopy with Ge-prism [19,20]. Realisation of polarisation rotation on the sample stage is established in visible light polariscopy, where it is based on an electrically controlled optical phase retardance in a liquid crystal cell [21].

The high sensitivity ATR detection is realised with multi-reflection slabs/prisms where the number of reflections from the sample-prism interface can increase more than ten times [24]. Amplitude and phase changes for such a situation becomes cumulative and reflection (for E-field) can be expressed as [25]:

$$\tilde{r}(\omega) = \frac{n_1 - [n(\omega) + ik(\omega)]}{n_1 + [n(\omega) + ik(\omega)]} \equiv r(\omega)e^{i\theta(\omega)}, \quad (5)$$

where  $n_1$  is the refractive index of the ATR prism,  $\tilde{n}(\omega) = n(\omega) + ik(\omega)$  is the complex index of the sample,  $r(\omega) = \sqrt{R(\omega)}$  is the field reflection coefficient calculated from the experimentally measured reflectance  $R$  spectrum, and  $\theta$  is the phase change introduced by the ATR prism. The refractive index  $\tilde{n} = n + ik$  of the sample is then [25]:

$$n = \frac{1 - r^2}{1 + r^2 + 2r \cos \theta} \times n_1; \quad k = \frac{-2r \sin \theta}{1 + r^2 + 2r \cos \theta} \times n_1, \quad (6)$$

and can be determined at each wavelength where reflectivity  $r(\omega)$  was measured, while the phase  $\theta(\omega)$  is derived via Kramers-Kronig relation from  $r(\omega)$ . It is usually possible to calculate the reflectivity and phase changes from a single reflection for the entire number  $N$  of reflections (see Eqn. 5) as

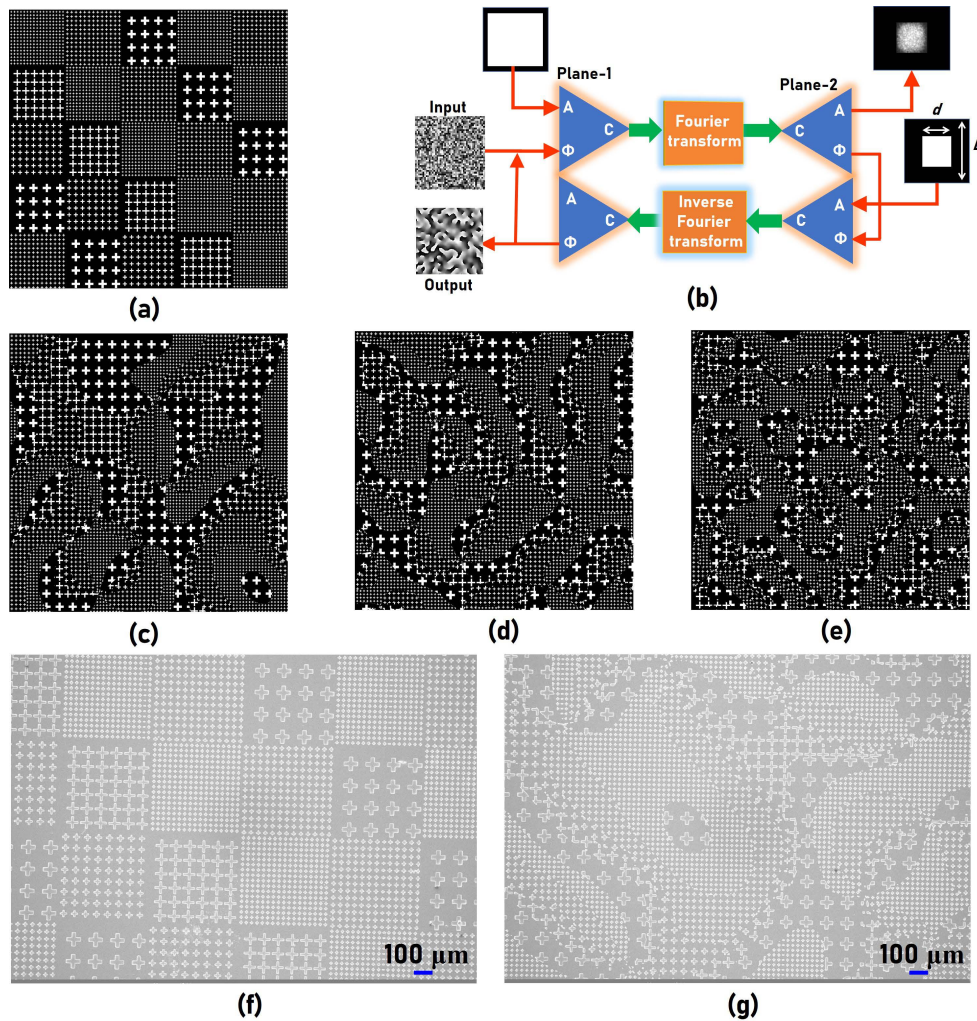


**Figure 8.** (a) Image of super-pixel mosaic design with  $5 \times 5$  elements. (b) A block scheme of the Gerchberg-Saxton Algorithm with scattering degree  $\sigma = d/D$ . Images of spatially randomly multiplexed cross-filters with for (c)  $\sigma = 0.1$ , (d)  $\sigma = 0.15$  and (e)  $\sigma = 0.2$ . SEM images of the fabricated (f) mosaic type and (g) randomly-multiplexed cross filters on gold coated SU8 films on silicon substrate.

$\tilde{r}(\omega) = [r_{one}(\omega)]^N \times e^{iN\theta_{one}(\omega)}$ , where  $r_{one}$  and  $\theta_{one}$  are the corresponding changes occurring at the single reflection [26].

### 3.5. Combined spectral filters and polarisers

A toolbox of spectral filters and polarisers are required to fully explore the potential of spectroscopy for material characterisation. Such a toolbox is less developed for the THz spectral range. However, due to low resolution photo-lithography required for longer sub-mm wavelengths, spectral filters can be easily made based on a square lattice (Fig. 7(a)). For the chosen wavelength  $\lambda_{THz}$  [ $\mu\text{m}$ ] the period  $P = 0.78393 \times \lambda_{THz}$ , the length of cross opening  $L = 0.1482 \times \lambda_{THz}$ , the width of the opening  $W = 0.50897 \times \lambda_{THz}$  [22]. The typical 10 – 15% bandwidth  $\Delta\lambda/\lambda_0$  for the geometry defined above becomes smaller as the  $P/L$  and  $P/W$  ratios are increased while the center frequency of band-pass filter is mainly dependent on the cross-member length  $L$ . It was demonstrated that transmission  $T > 0.9$  can be obtained using micrometers-thick Cu-foil within 0.5-2 THz spectral range using the presented scaling [22].

With the known spectral profile of the synchrotron source (inset of Fig. 7(b)), it is possible to design a transmission mask which will filter spectral bands and sets their intensities. Such filters were

numerically designed to produce a comb of THz frequencies (five for the pattern shown in Fig. 7(b)). As is known, it is desirable to have a uniform spectral response such that the gain of the bolometer can be precisely set in advance. The spectral profile can be precisely engineered by spatially multiplexing cross-filter designs corresponding to different wavenumbers. The first method is a super-pixel type spatial multiplexing where every pixel of the mask is formed by the mosaic of the building block of the different filters. A super-pixel design with  $5 \times 5$  elements is shown in Fig. 8(a). This is the most straightforward approach but results in undesirable diffraction orders due to the periodic configuration. The second approach uses a random phase mask. In principle, any random phase mask will work but in order to allow at least certain number of crosses of the same type, it is crucial to engineer the scattering ratio of the random phase mask. Such quasi-random phase masks can be synthesized using the well-known Gerchberg Saxton algorithm (GSA) by giving the scattering ratio as input [27]. The schematic of the GSA is shown in Fig. 8(b). The algorithm begins with a complex amplitude consisting of a uniform amplitude and random phase function at plane - 1 which is Fourier transformed. The amplitude in plane - 2 is replaced by a uniform amplitude within a predefined area which decides the scattering degree given as  $\sigma = d/D$ , where  $d$  is the length of the predefined area and  $D$  is the length of the total area. The output of the GSA is a quasi-random phase mask consisting of grey levels from 0 to  $2\pi$ . As the area of every different phase level is equal, different grey level ranges can be set to different filters. By controlling the relative ranges, the relative intensity responses can be manipulated. The images of a section of spatially randomly multiplexed cross-filters for  $\sigma = 0.1$ ,  $\sigma = 0.15$  and  $\sigma = 0.2$  are shown in Fig. 8(c), Fig. 8(d) and Fig. 8(e), respectively. Use of photolithography on thick 20-500  $\mu\text{m}$  SU8 laminates (SU8 from DJ Microlaminates Ltd.) is particularly appealing due to possibility to retrieve free standing mesh filters. With gold (or any other metal) coating this would complete the filter. The SEM images of the mosaic type comb type and randomly multiplexed cross-filters on gold coated SU8 films on Silicon substrate are shown in Fig. 8(f) and Fig. 8(g) respectively. Due to the an isotropic geometry of cross and symmetry of the square lattice, isotropic polarisation response is expected [28]. Polarisation active filters can be fabricated using the same approach.

#### 4. Conclusions and Outlook

In this prospective/concept paper analysis of ATR measurements is presented with most of the examples based on experiments at the THz beamline at the Australian Synchrotron. Explicit formulae pertinent to the ATR data analysis is presented for the discussion and illustration of practical examples as well as tutorial value. Challenges to use THz ATR units for polarisation analysis is due to a large number of internal reflections: five to the ATR prism and extra five to the output port. Moreover, focusing is carried out on the beam propagation to the sample and those reflections have complex angular dependence and distribution of angles of incidence. This is additionally complicated by complex polarisation composition of the synchrotron beam. However, for the unique spectral window at  $< 3$  THz where table top THz sources are not available for high brilliance/intensity, synchrotron polarisation is mostly linear ( $\sim 90\%$ ; along the slit of the first mirror used to extract THz radiation from the synchrotron) and can be utilised for THz polariscopy, which is still at the very early stage of development. Debye rotation, network stretching, rocking and wagging librations of water molecules all are active at low-THz spectral band [29]. Spectral filters for specific spectral bands can be made using photolithography on free-standing SU8 laminates as shown above. Metal coating of developed SU8 micro-sheets can produce single frequency transmission filters as well as intensity and bandwidth comb-filters.

The 4-Pol method's potential with the ATR mode and development of spectral/polarisation filters is presented by concept examples. In addition, polarisation optics for spin and orbital angular momentum (SAM and OAM) of THz radiation has to be developed for interrogation of complex orientational structures, especially in biological/medical samples. Due to a high transparency of Si at THz spectral band and readily available Si plasma etching for high aspect ratio structures, optical elements such as a optical vortex generators for SAM-OAM manipulation at THz frequencies can

be made [30]. Long wavelength (low frequency) optical radiation is promising for opto-mechanical applications [31–37]. Indeed, the reaction torque exerted onto an object by a beam of power  $P$  is  $\Gamma = \Delta\sigma P/\omega$ , where  $\Delta\sigma$  is the before-after change of the circular polarisation state [38].

**Funding:** This work was supported by JST CREST Grant Number JPMJCR19I3, Japan, and the ARC Discovery DP190103284 grants. The project was carried during EU16010, M15121 beamtimes at the Australian Synchrotron. ZV and AWW are grateful for support via NHMRC grant 1042464. SJ and SHN are grateful to support via ARC Linkage LP190100505 project.

**Conflicts of Interest:** The authors declare no conflict of interest.

## References

1. Zhang, W.; Nickel, D.; Mittleman, D. High-pressure cell for terahertz time-domain spectroscopy. *Optics Express* **2017**, *25*, 2983–2993.
2. Vij, J.; Simpson, D.; Panarina, O. Far infrared spectroscopy of water at different temperatures: GHz to THz dielectric spectroscopy of water. *J. Molecular Liquids* **2004**, *112*, 125–135.
3. Ryu, M.; Linklater, D.; Hart, W.; Balcytis, A.; Skliutas, E.; Malinauskas, M.; Appadoo, D.; Tan, Y.; Ivanova, E.P.; Morikawa, J.; Juodkazis, S. 3D printed polarizing grids for IR-THz synchrotron radiation. *J. Opt.* **2018**, *20*, 035101.
4. Ramer, G.; Lendl, B., Attenuated Total Reflection Fourier Transform Infrared Spectroscopy. In *Encyclopedia of Analytical Chemistry: online*; John Wiley and Sons, Ltd.: Berlin, Germany, 2013.
5. Yu, A.; Zhu, S.; Roy, R. Variable transmission output coupler and tuner for ring laser systems. *Applied Optics* **1985**, *24*, 3610–3614.
6. Vilagosh, Z.; Lajevardipour, A.; Appadoo, D.; Ng, S.H.; Juodkazis, S.; Wood, A. Characterisation of Biological Materials at THz Frequencies by Attenuated Total Reflection: Lard. *Appl. Sci.* **2020**, *10*, 8692.
7. Vilagosh, Z.; Lajevardipour, A.; Appadoo, D.; Juodkazis, S.; Wood, A. Using Attenuated Total Reflection (ATR) Apparatus to Investigate the Temperature Dependent Dielectric Properties of Water, Ice, and Tissue-Representative Fats. *Appl. Sci.* **2021**, *11*, 2544.
8. Hasted, J.; Husain, S.; F.A.M.Frescura.; J.R.Birch. The temperature variation of the near millimetre wavelength optical constants of water. *Infrared Physics* **1987**, *27*, 11–15.
9. Liebe, H.; Hufford, G.; Manabe, T. A model for the complex permittivity of water at frequencies below 1 THz. *Int J Infrared Millimeter Waves* **1991**, *12*, 659–675.
10. Zhang, C.; Lee, K.; Zhang, X.; Wei, X.; Shen, Y. THz spectroscopy of ice. *Lasers Electro-Optics Society IEEE* **2002**, *2*, 646–647.
11. Møller, U.; Folkenberg, J.; Jepsen, P. Dielectric properties of water in butter and water–AOT–heptane systems measured using terahertz time-domain spectroscopy. *Applied spectroscopy* **2010**, *64*, 1028–1036.
12. Zheng, Y.; Rosa, L.; Thai, T.; Ng, S.H.; Juodkazis, S.; Bach, U. Phase controlled SERS enhancement. *Scientific Reports* **2019**, *9*, 744.
13. Jayawardhana, S.; Rosa, L.; Juodkazis, S.; Stoddart, P.R. Additional Enhancement of Electric Field in Surface-Enhanced Raman Scattering due to Fresnel Mechanism. *Sci. Rep.* **2013**, *3*, 2335.
14. Rogalin, V.E.; Kaplunov, I.A.; Kropotov, G.I. Optical Materials for the THz Range. *Optics and Spectroscopy* **2018**, *125*, 1053–1064.
15. Hikima, Y.; Morikawa, J.; Hashimoto, T. FT-IR Image Processing Algorithms for In-Plane Orientation Function and Azimuth Angle of Uniaxially Drawn Polyethylene Composite Film. *Macromolecules* **2011**, *44*, 3950–3957.
16. Honda, R.; Ryu, M.; Balcytis, A.; Vongsvivut, J.; Tobin, M.J.; Juodkazis, S.; Morikawa, J. Paracetamol micro-structure analysis by optical mapping. *Appl.Surf. Sci.* **2019**, *473*, 127–132.
17. Honda, R.; Ryu, M.; Moritake, M.; Balcytis, A.; Mizeikis, V.; Vongsvivut, J.; Tobin, M.J.; Appadoo, D.; Li, J.L.; Ng, S.H.; Juodkazis, S.; Morikawa, J. Infrared Polariscopy Imaging of Linear Polymeric Patterns with a Focal Plane Array. *Nanomaterials* **2019**, *9*, 732.
18. Honda, R.; Ryu, M.; Moritake, M.; Balcytis, A.; Mizeikis, V.; Vongsvivut, J.; Tobin, M.J.; Appadoo, D.; Li, J.L.; Ng, S.H.; Juodkazis, S.; Morikawa, J. Hyperspectral mapping of anisotropy. *Nanoscale Horizons* **2019**, *4*, 1443–1449.

19. Ryu, M.; Balčytis, A.; Wang, X.; Vongsvivut, J.; Hikima, Y.; Li, J.; Tobin, M.J.; Juodkazis, S.; Morikawa, J. Orientational Mapping Augmented Sub-Wavelength Hyper-Spectral Imaging of Silk. *Sci. Reports* **2017**, *7*, 7419.
20. Ryu, M.; Kobayashi, H.; Balcytis, A.; Wang, X.; Vongsvivut, J.; Li, J.; Urayama, N.; Mizeikis, V.; Tobin, M.; Juodkazis, S. Nanoscale chemical mapping of laser-solubilized silk. *Mater. Res. Express* **2017**, *4*, 115028.
21. Honda, R.; Ryu, M.; Li, J.L.; Mizeikis, V.; Juodkazis, S.; Morikawa, J. Simple multi-wavelength imaging of birefringence: case study of silk. *Sci. Rep.* **2018**, *8*, 17652.
22. Porterfield, D.W.; Hesler, J.L.; Densing, R.; Mueller, E.R.; Crowe, T.W.; ; Weikle, R.M. Resonant metal-mesh bandpass filters for the far infrared. *Applied Optics* **1994**, *33*, 6046–6052.
23. Balčytis, A.; Ryu, M.; Wang, X.; Novelli, F.; Seniutinas, G.; Du, S.; Wang, X.; Li, J.; Davis, J.; Appadoo, D.; Morikawa, J.; Juodkazis, S. Silk: Optical Properties over 12.6 Octaves THz-IR-Visible-UV Range. *Materials* **2017**, *10*, 356.
24. Minnes, R.; Nissinmann, M.; Maizels, Y.; Gerlitz, G.; Katzir, A.; Raichlin, Y. Using Attenuated Total Reflection–Fourier Transform Infra-Red (ATR-FTIR) spectroscopy to distinguish between melanoma cells with a different metastatic potential. *Scientific Reports* **2017**, *7*, 4381.
25. Okamura, H. A simple method for the Kramers-Kronig analysis of reflectance spectra measured with diamond anvil cell. *J. Phys.: Conf. Ser.* **2012**, *359*, 012013.
26. Harrick, N.J. *Internal Reflection Spectroscopy*; Harrick Scientific Corporation: Ossining, NY, 1979.
27. Yang, G.Z.; Dong, B.Z.; Gu, B.Y.; Zhuang, J.Y.; Ersoy, O. Gerchberg–Saxton and Yang–Gu algorithms for phase retrieval in a nonunitary transform system: a comparison. *Appl. Opt.* **1994**, *33*, 209–218.
28. Balčytis, A.; Ryu, M.; Seniutinas, G.; Nishijima, Y.; Hikima, Y.; and, M.Z. Si-based infrared optical filters. *Opt. Eng.* **2015**, *54*, 127103 – 127103.
29. Novelli, F.; Guchhait, B.; Havenith, M. Towards Intense THz Spectroscopy on Water: Characterization of Optical Rectification by GaP, OH1, and DSTMS at OPA Wavelengths. *Materials* **2020**, *13*, 1311.
30. Dharmavarapu, R.; Izumi, K.I.; Katayama, I.; Ng, S.; Vongsvivut, J.; Tobin, M.; Kuchmizhak, A.; Nishijima, Y.; Bhattacharya, S.; Juodkazis, S. Dielectric cross-shaped-resonator-based metasurface for vortex beam generation at mid-IR and THz wavelengths. *Nanophotonics* **2019**, *8*, 1263–1270.
31. Juodkazis, S.; Mukai, N.; Wakaki, R.; Yamaguchi, A.; Misawa, H. Reversible Phase Transitions in Polymer gels Induced by Radiation forces. *Nature* **2000**, *408*, 178–181.
32. Brasselet, E.; Murazawa, N.; Misawa, H.; Juodkazis, S. Optical vortices from liquid crystal droplets. *Phys. Rev. Lett.* **2009**, *103*, 103903.
33. Brasselet, E.; Malinauskas, M.; Žukauskas, A.; Juodkazis, S. Photo-polymerized microscopic vortex beam generators : precise delivery of optical orbital angular momentum. *Appl. Phys. Lett.* **2010**, *97*, 211108.
34. Misawa, H.; Juodkazis, S. Photophysics and photochemistry of a laser manipulated microparticle. *Progress Polymer Science* **1999**, *24*, 665–697.
35. Sun, Q.; Juodkazis, S.; Murazawa, N.; Mizeikis, V.; Misawa, H. Freestanding and movable photonic microstructures fabricated by photopolymerization with femtosecond laser pulses. *J. Micromech. Microeng.* **2010**, *20*, 035004/1–5.
36. Takasone, T.; Juodkazis, S.; Kawagishi, Y.; Yamaguchi, A.; Matsuo, S.; Sakakibara, H.; Nakayama, H.; Misawa, H. Flexural Rigidity of a Single Microtubule. *Jpn. J. Appl. Phys.* **2002**, *41*, 3015–3019.
37. Juodkazis, S.; Shikata, M.; Takahashi, T.; Matsuo, S.; Misawa, H. Fast Optical Switching by a Laser Manipulated Microdroplet of Liquid Crystal. *Appl. Phys. Lett.* **1999**, *74*, 3627–3629.
38. Juodkazis, S.; Mizeikis, V.; Matsuo, S.; Ueno, K.; Misawa, H. Three dimensional micro- and nano-structuring of materials by tightly focused laser radiation. *Bulletin Chemical Society Japan* **2008**, *81*, 411–448.
39. P.A.Flournoy.; W.J.Schaffers. Attenuated total reflection spectra from surfaces of anisotropic, absorbing films. *Spectrochimica Acta* **1966**, *22*, 5–13.

## Appendix A Phase and amplitude changes in ATR

The amplitude and phase of reflected light from the diamond prism interface with the sample changes (Eqn. 4) and has to be accounted for in the analysis of light using analyser. First, the changes

without sample (from ATR prism-air interface) are considered at different angle of incidence  $\theta_i$ . The reflectivity of the TM and TE modes is following [39]:

$$\ln R_{TE}(\theta_i) = - \frac{4n_2^2 k_2}{n_1^2 \tan(\theta_i) \sqrt{1 - \frac{n_2^2}{n_1^2 \sin^2 \theta_i} \times \left(1 - \frac{n_2^2}{n_1^2}\right)}}, \quad (\text{A1})$$

$$\ln R_{TM}(\theta_i) = - \frac{4n_2^2 \left(2 - \frac{n_2^2}{n_1^2 \sin^2 \theta_i}\right) k_2}{n_1^2 \tan \theta_i \sqrt{1 - \frac{n_2^2}{n_1^2 \sin^2 \theta_i} \left(1 - \frac{n_2^2}{n_1^2 \sin^2 \theta_i} + \frac{n_2^4}{n_1^4} \cot^2 \theta_i\right)}}, \quad (\text{A2})$$

where  $n_1 = 2.12$  is the refractive index of the ATR prism (medium 1) and  $n_2 + ik_2$  (medium 2) is the sample (or air  $n_2 = 1$ ) for the THz spectral range. Reflectivity at the interface changes amplitude of the  $E_{s,p}$  fields which are detected by the analyser. Also, the phase changes upon ATR depending on the angle according to the Fresnel formulas defined for the relative refractive index  $n = n_2/n_1$ :

$$\phi_{TE}(\theta_i, n) = -2 \tan^{-1} \left( \frac{\sqrt{\sin^2 \theta_i - n^2}}{\cos \theta_i} \right), \quad (\text{A3})$$

$$\phi_{TM}(\theta_i, n) = \pi - 2 \tan^{-1} \left( \frac{\sqrt{\sin^2 \theta_i - n^2}}{n^2 \cos \theta_i} \right), \quad (\text{A4})$$

for the  $\theta_i > \theta_c$  where the critical angle  $\theta_c = \sin^{-1}(n)$ ; reflection is internal when  $n < 1$ . The evanescent field depth  $1/\alpha$  is defined by the absorption coefficient  $\alpha = \frac{2\pi}{k} \sqrt{\frac{\sin^2 \theta_i}{n} - 1}$  (for  $n < 1$ ).

The Fresnel formulas shown above are plotted in Fig. A1. Reflectivity does not change the amplitude of reflected TE and TM modes at angles of incidence larger than the critical angle  $\theta_c$  (Fig. A1(a)). Absorption of THz beam due water humidity can be modeled by increasing the imaginary part of the refractive index  $k_2$  (see solid vs dashed lines in (a)). The phase change upon reflection of TE

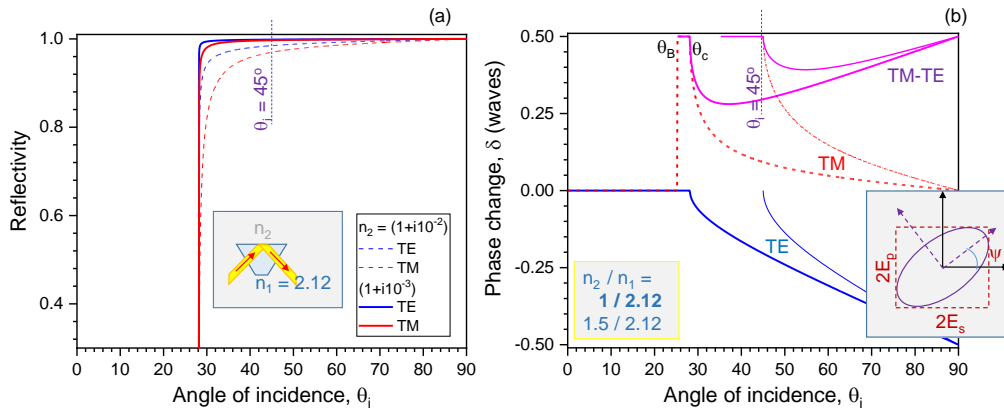


**Figure A1.** Visualisation of Eqns. A1-A4. Reflection coefficients  $R_{TE,TM}$  vs. angle of incidence  $\theta_i$  for the ATR prism, e.g.,  $n_1 = 2.12$  at THz spectral range. Absorption in air is added by the imaginary part of refractive index  $k_2 = 10^{-2}$  and  $10^{-3}$ . Inset shows ATR geometry and conventions. (b) The phase change upon reflection for the TE and TM modes governed by the real part of refractive indices  $n = n_2/n_1$ . The polarising Brewster angle is given by  $\theta_B = \tan^{-1}(n)$  and the critical angle  $\theta_c = \sin^{-1}(n)$ . Thinner lines correspond to the case when the sample has a refractive index of  $n_2 = 1.5$ . The right-inset in (b) shows the polarisation ellipse after the analyser.

and TM modes experiences complex changes at the polarising Brewster and critical angles (Fig. A1(b)). Most importantly, the phase differences for the TM and TE modes experiences the largest phase change close to the  $\lambda/4$  condition for  $\theta_i = 35 - 45^\circ$ . Typical ATR setups are designed for  $\theta_i \approx \pi/4$ , hence, a strong phase difference is expected due to reflection from the sample-diamond interface, depending to the refractive index contrast  $n$ ; see thinner lines in Fig. A1(b) which represent phase changes for  $n = n_2/n_1 = 1.5/2.12$ .

Upon reflection from the diamond-sample interface, both amplitudes of the  $E_z$  (TM) and  $E_y$  (TE) components can be changed because of anisotropy of absorption, which is additionally affected by the phase change between TM and TE modes, and is solely defined by the refractive index ratio at the interface. For the coherent E-field addition, the reflected light is elliptically polarised and can be expressed in s-/p-components measurable with analyser (inset in Fig. A1(b)). The ratio of s- and p-components of E-field  $\tan \beta = E_p/E_s$  and the phase difference upon reflection  $\delta$ . The polarisation ellipsis is expressed by two angular parameters: the orientation angle  $\psi'$  and the ellipticity angle  $\chi'$  as  $\tan(2\psi') = \tan(2\beta) \times \cos(\delta)$  and  $\tan(2\chi') = \sin(2\beta) \times \sin(\delta)$ . This polarisation change is mainly defined by the phase change  $\delta$  upon reflection. For the incoherent light case, intensities of the two components  $E_p^2$  and  $E_s^2$  are added (Eqn. 4).